

Rock type prediction and 3D modeling of clastic paleokarst fillings in deeply-buried carbonates using the Democratic Neural Networks Association technique

José N. Méndez^a, Qiang Jin^a, Xudong Zhang^a, María González^b, Muhammad Kashif^c, Cyril D. Boateng^a, Miller Zambrano^d

^a China University of Petroleum (East China), China

^b Emerson Automation Solutions, Brazil

^c University of Sargodha, Pakistan

^d University of Camerino, Italy

ARTICLE INFO

Keywords:

Clastic paleokarst fillings
Rock type prediction
3D facies modeling
Democratic neural networks association technique

ABSTRACT

This study outlines a probabilistic model based on artificial neural networks applied to the deeply-buried karsted carbonates of the Ordovician Yingshan Formation, which represent significant oil reservoirs in western China. The complexity of both rock type prediction and 3D facies modeling of paleokarst fillings, which are hosted within the cavities, drives the need to apply innovative techniques for identifying new oil plays. Due to the high heterogeneity of clastic fillings and patchy continuity of the karst patterns, physical evaluation of these reservoirs is extremely complex. We propose the Democratic Neural Networks Association (DNNA) as the probabilistic technique to solve these challenges. This technique simultaneously runs several artificial neural networks in parallel and combines seismic data and well logs. The resulting probable facies volume is expected to provide an appropriate distribution and delineation of clastic fillings (i.e., conglomerates, fine-grained sandstones, siltstones, mudstone, dolomite fragments, and sparry calcarenite) and unfilled or empty spaces. This calculated volume is then used as a reliable input data to condition trend analysis on a very fine geological grid, in order to model the complex patterns in question. The static model obtained shows that, the probabilistic distribution of each filling has the same orientation as karst system. Likewise, spatial dimensions similar to the proposed analogue model of these patterns (vertical and horizontal scales) are delineated. Finally, we validated prediction results by comparing them with the interpreted karst facies of a well not initially considered in the 3D model. The results indicating that the DNNA technique proves to be a useful innovative tool for generating realistic depictions of fillings deposited within deeply-buried paleokarst.

1. Introduction

In recent years, artificial neural networks have undergone a renaissance in oil and gas industry (Ali, 1994; Elshafei and Hamada, 2007; Alkinani et al., 2019). Many researchers have been inspired to report their results using different models with oil and gas exploration data (Elshafei and Hamada, 2007). Although various methods have been developed to speed up interpretation and improve prediction, significant challenges still exist, e.g., in seismic facies classification (Liu et al., 2020). Several studies have approached rock facies classification using artificial neural networks with petrophysical features (well logs data) as

input data (Hall, 2016; Chen and Zeng, 2018; Shashank and Mahapatra, 2018; Chevitaresh et al., 2020). In a similar vein, other researchers have combined these algorithms with seismic data to predict or interpret geometries of sediments elements, for examples Saggaf et al. (2003), Zhao (2018), Di et al. (2019), Boateng et al. (2020), Liu et al. (2020). Their conclusions include a fairly precise seismic facies characterization in siliciclastic environments. However, predicting paleokarst fillings hosted in deeply-buried carbonates, the seismic-based facies classification is not yet decisive.

Many studies have used artificial neural networks tools to describe karst as oil reservoirs or aquifers (Lin et al., 2013; Kong-A-Siou et al.,

E-mail addresses: jnmendez25@gmail.com (J.N. Méndez), jinqiang@upc.edu.cn (Q. Jin), 496349624@qq.com (X. Zhang), maria.g.gonzalez@emerson.com (M. González), kashifyaqub@yahoo.com (M. Kashif), cyrilboat@yahoo.com (C.D. Boateng), miller.zambrano@unicam.it (M. Zambrano).

<https://doi.org/10.1016/j.marpetgeo.2021.104987>

Received 2 November 2020; Received in revised form 30 January 2021; Accepted 16 February 2021

Available online 20 February 2021

0264-8172/© 2021 Elsevier Ltd. All rights reserved.

2015; Chen and Zeng, 2018; Kovačević et al., 2020; Xin et al., 2020). These robust techniques have been running in oilfields to predict the morphology and continuity of the karst patterns. However, the karst fillings interpretation still represents a significant challenge due to limitations for successfully implementing of learning strategies from hard data samples of seismic data. In addition, the size of seismic volume and available well data (qualified population) are factors that can limit the training set in terms of diversity. Even though the seismic dataset permits the relative visualization of karst features, the resolution limits rock types' discretization that fill these cavities. Therefore, it is difficult estimating and modeling the types of paleokarst fillings related to reservoirs. This complexity drives the need to apply recent and innovative techniques with a probabilistic approach to reduce geological uncertainty. This new study estimates the probabilistic distribution and spatial sorting of the lithofacies that compose the clastic paleokarst fillings in the karsted carbonates. We have opted to carry out this challenge after several tests using, the Democratic Neural Networks Association (DNNA) technique that combines well logs and seismic data (Hami-Eddine et al., 2015; De Ribet, 2016).

The DNNA technique is an artificial method that associates multiple training cycles to generate lithological probabilities from the combination of quantitative rock typing analysis at wells locations and in the seismic dataset (Hami-Eddine et al., 2015). Generally, this technique has been previously used to estimate lithological distributions related to siliciclastic and carbonates rocks (Hastie et al., 2009; Hami-Eddine et al., 2015; De Ribet, 2016). The probabilistic approach of DNNA combines all seismic-related information to compute a probable facies volume (distribution and propagation). As a different learning strategy, the DNNA technique simultaneously runs different neural networks trained with the same hard data set (Zhou and Goldman, 2004). This approach provides the ability to handle associative neural networks' training with a unique set of seismic data attributes that are not necessarily independent or paired with the well information (Hami-Eddine et al., 2015). Additionally, this technique permits the supervised addition of soft data from the seismic dataset to improve the training (democratic contribution). The well information consists of discrete facies described from core and cutting samples and electrofacies logs processed from multi-regression analysis of selected well logs.

Another objective in this investigation is building a geocellular model that considers an appropriate distribution of the clastic fillings inside and along cavities. Many authors have modeled karst features highlighting the differences between karst zones using robust techniques (Liu et al., 2008; Zhao et al., 2008; Lu et al., 2012; Li et al., 2016; Tian et al., 2016; Méndez et al., 2020 b). However, our 3D facies modeling proposal goes further and tries to simulate the lithological heterogeneities in a probabilistic way. Using the most probable facies volume obtained from the DNNA technique and well information as input data in trend analysis, we can model the highly heterogeneous fillings can be modeled. We expect the resulting realization of the model to evaluate the reproduced trends and represent the correct spatial interaction between different lithofacies.

Generally, clastic paleokarst fillings consist of random deposits in the karst system of both siliciclastic and carbonates sediments transported by underground rivers and/or streams (Jin et al., 2015a; Li, 2017). For this case study, the fillings hosted within the Ordovician Yingshan Formation carbonates represent relevant deeply-buried reservoirs for oil and gas production in the Tahe oilfield, western China (Xiao et al., 2003; Chen and Wei, 2010; Yang et al., 2011; Zhao et al., 2014; Yu et al., 2018; Méndez et al., 2020a). Multi-dissolution stages and erosion produced the karst system in this area due to tectonic events in the middle Caledonian and late Hercynian orogenies (Chen et al., 2012; Li, 2017). The characteristic of these karsted carbonates can be visualized along the T₇₄ unconformity (Li, 2017). Different rock types filled some cavities during and after the karstification processes (Dell'Oca, 1961; Loucks and Anderson, 1985; Loucks, 1999, 2001; Jin et al., 2015a; 2015b; Tian et al., 2016, 2017).

Furthermore, we take into account a recently reprocessed seismic dataset that improves the Paleozoic targets' seismic resolution seismic resolution in the study area. This dataset provides users with enhanced comprehensive information on the stratigraphic features of the karst system. Finally, this entire workflow's results represent a significant contribution to geoscientific knowledge on the geological characterization of karsted carbonate reservoirs.

2. Geological settings

The study area covers 13.5 km², with a total of 13 wells (TK210, TK211, T403, TK405, TK408, TK410, TK411, TK419, TK428, TK446, TK458H, TK476 and TK467) drilled in operating zones 2 and 4 of the Tahe oilfield within the Tarim Basin (Fig. 1). In this region, paleokarst fillings associated with clastic sediments were determined based on outcrops, wireline logs and core samples (Jin et al., 2015a; Tian et al., 2016; Wu et al., 2018; Méndez et al., 2019). The study area is structurally located on the southwestern slope of the south-central Tabei uplift, an ancient tectonic structure where the deformation occurred in several periods mainly during the Caledonian and Hercynian orogeny (Chen and Wei, 2010; Li, 2017). During these orogenies, the paleomorphology consisted of a karst landscape affected by multi-stages of karstification (Fig. 2). Processes related to meteoric waters and burial and hydrothermal activities produced by carbonate dissolution (Loucks, 1999; He et al., 2010; Chen et al., 2012).

The first karstification stage in the middle Caledonian affected the Ordovician strata (Chen et al., 2012). This stage is described in three episodes designated as I, II and III (Chunyan, 2008; Chen et al., 2012; Tian et al., 2016), show in Fig. 2. The episode I occurred in the Middle Ordovician after the Yijianfang Formation deposition. In this episode, the stratigraphic unit was partially eroded, developing scattered syngenetic pores by karstification (Jin et al., 2015a; Tian et al., 2016). Episodes II and III originated in the Upper Ordovician after the Lianglitage (O₃l) and Sangtamu (O₃s) Formation depositions (Fig. 2), small cavities in Ordovician strata were produced (Li, 2017). In the early Hercynian stage, the last and more drastic karstification process occurred on the Ordovician carbonate platform, due to its long duration and widespread distribution (Tian et al., 2016; Chen et al., 2012; Li, 2017). This process is the source of the main paleokarst elements identified in the study area (Changsong, 2011; Yang et al., 2011). At this late-stage, the karstification process includes the dissolution and transformation of the early-stage karstification attributes, to form complex karst features (Li, 2017; Tian et al., 2016). The developed karst zones then control hydrocarbon accumulation in the Tahe area (Zeng et al., 2010).

2.1. The Yingshan Formation carbonates and types of paleokarst fillings

The Ordovician Yingshan Formation is the key stratigraphic unit and is generally composed of carbonates rocks such as grainstone and dolomitic limestone (Liu et al., 2008; Chen et al., 2012; Zhao et al., 2014; Li et al., 2018, Fig. 2). We find these karsted carbonates in certain areas of the Tarim Basin. The karsted section of the Yingshan Formation is visible in the seismic reflection window between 3400 and 4000 ms. However, the key interval covers 118-ms (~250-m) between the seismic horizons of T₇₄ and T₇₆ unconformities (Chen et al., 2012). Within this time window, various patterns similar to karst geomorphology have been visualized (Fig. 3). The karst system represented here as cavities with tubular shapes and asymmetrical geometry are oriented structurally along the strike of several faults (Zeng et al., 2010; Zhang et al., 2012). In these cavities, the clastic paleokarst fillings produced by mechanical erosion or incision processes, such as underground rivers or streams (Zeng et al., 2010), were sedimented or deposited. The sediments were sourced from the northwestern platform and subsequently consolidated in rock packages such as polymictic conglomerates, calcareous sandstones, siltstones, sparry calcarenite, and mudstones

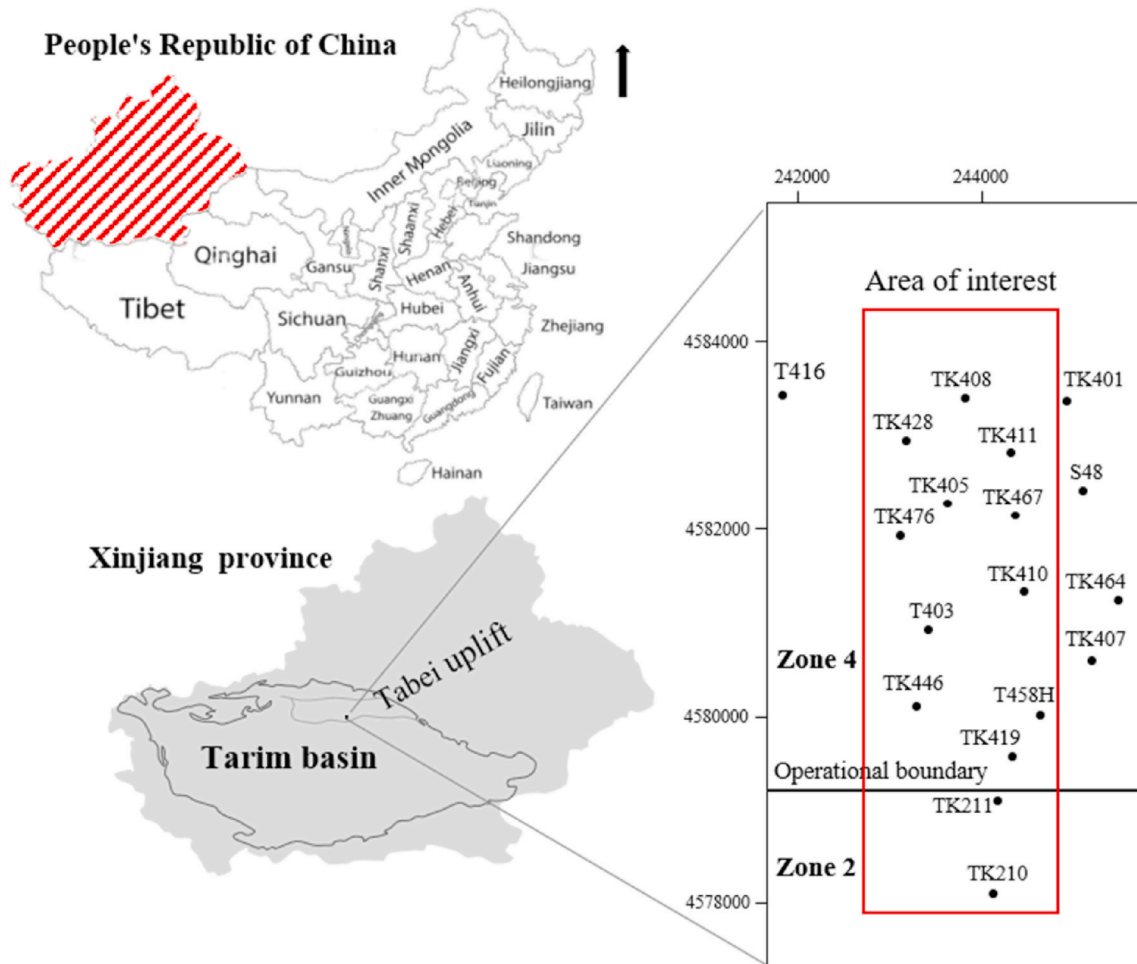


Fig. 1. Geographical location of the study area covering 2 operational zones in the Tahe oilfield, Tarim basin, western China.

(Zeng et al., 2010; Zhang et al., 2012; Tian et al., 2017; Wu et al., 2018). Fig. 4 shows several lithofacies.

Fig. 5a shows an analogue model of these clastic fillings deposited in a paleocave with the following dimensions >5 m (width) x 3.2 m (height). Li et al. (2014) also observed cavities with approximate dimensions of 16 m (wide) x 3.1 m (height). But in the outcrops, the fillings are usually composed of limestone blocks sub-rounded clasts larger than 3 cm radius and siliciclastic debris flows arranged in layers with sub-horizontal graded bedding. A conceptual model is shown in Fig. 5b (Loucks and Anderson, 1985; Loucks, 1999, 2001) for a better understanding of the chaotic internal distribution of the fillings. Furthermore, Fig. 5c shows the vertical distribution diagram of fillings created using wireline logs of well TK604. The borehole image log shown in Fig. 5c displays the detected vertical lithological changes within the karst based on resistivity variations. However, the mudstone and dolomite limestone lithofacies are best recognized through cutting samples and well logs. In particular cases, unfilled paleocaves stand out in well logs and outcrops.

On the other hand, clastic fillings exhibit frequent stacking and fining upward patterns in the well logs. These features match the sedimentary structures observed in outcrops, including graded bedding, which indicate the available accommodation space and sediment supply defines the cavity geometry (Mazullo and Chilingarian, 1996). In some instances, stacked patterns of calcarenites (mixed siliciclastic and carbonates) are found above the epikarst carbonate, representing the consolidated sediments of weathered crust (Wu et al., 2018).

3. Databases and methodology

The workflow is carried out in the Geolog™, SeisEarth®, and SKUA-GOCAD™ modules of the Paradigm Suite. A total of 10 wells with a suite of conventional wireline logs are available (TK211, T403, TK405, TK408, TK411, TK419, TK428, TK446, TK458H and TK476). To apply the DNNA technique, three poststack seismic attribute volumes are considered: acoustic impedance (P-wave data), relative acoustic impedance (RAI), and RMS amplitude (Fig. 6). These stratigraphic seismic attributes are selected according to the karst prediction studies carried out by Méndez et al. (2020 b). The main logs employed and calibrated in time are as follows: Gamma Ray (GR), Deep Resistivity (RD), Acoustic or Sonic (AC), Bulk Density (DEN), and Neutron (CNL). The Effective porosity (PHIE) and Permeability (Perm) curves are also considered in the processing of electrofacies logs. These last curves are calculated using the methods of Albery (1994) and Morris and Biggs (1967), respectively. In addition, the discrete facies log obtained from sedimentological descriptions of core samples and FMI's log features is available. We used this, to build a fine-scale geocellular grid that covers the followings dimensions, 10 × 10 m and 0.5 ms. Through the fine-scale geocellular grid is intended to capture the heterogeneities of fillings. The methodology for this study is divided into three stages: i) Computing electrofacies logs using Multi-Regression analysis; ii) Rock type prediction using the DNNA technique; and iii) 3D facies modeling.

3.1. Computing electrofacies logs using multi-regression analysis

The numerical combinations of wireline logs that reflect the physical

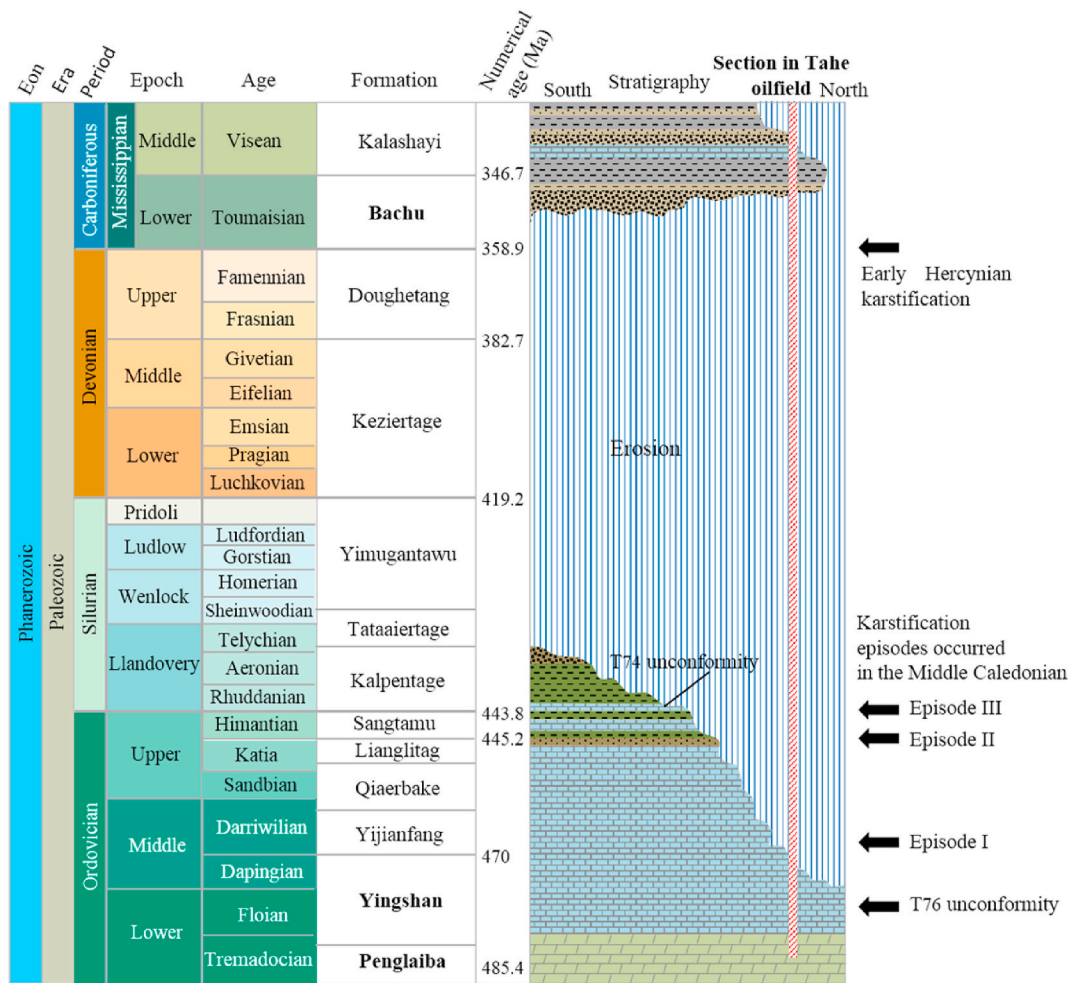


Fig. 2. Proposed stratigraphic column for the Tahe oilfield. Modified from Tian et al. (2016) and Mendez et al. (2020).

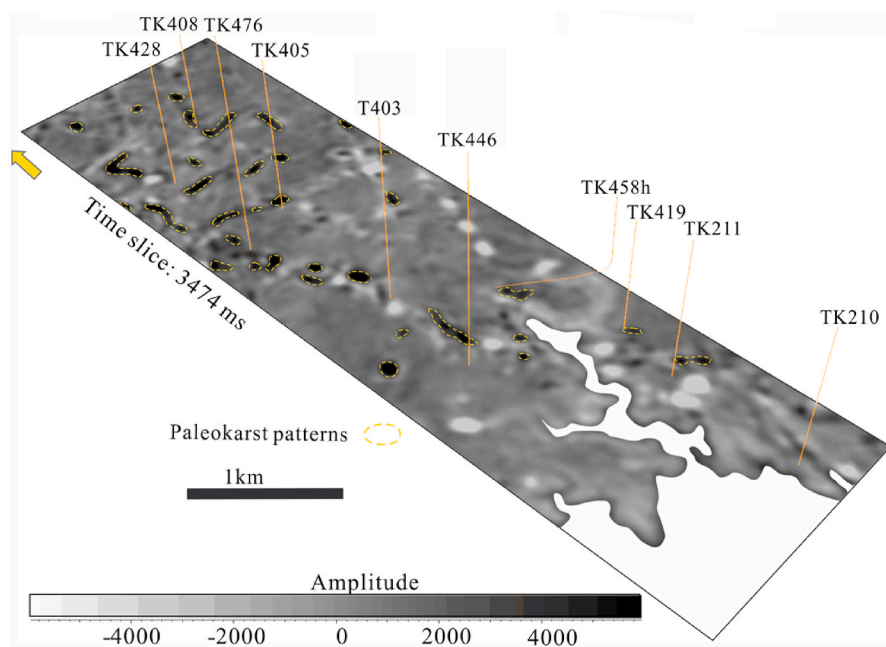


Fig. 3. Shapes of paleocaves (yellow dashed line) delineated in a time slice of the RMS amplitude seismic volume. The image shows how the morphology of the Ordovician karst system is configured in the study area. (For interpretation of the references to color in this figure legend, the reader is referred to the Web version of this article.)



Fig. 4. Different types of paleokarst fillings described in core samples; (a) T403–5537.6 m, the polymictic conglomerate fillings; (b) T615–5553.05 m, conglomerate fillings; (c) T615–5539.93 m, siltstone fillings; (d) T615–5557.84 m, calcareous sandstone fillings; and (e) S71–5504.4 m, conglomerate/calcarenite.

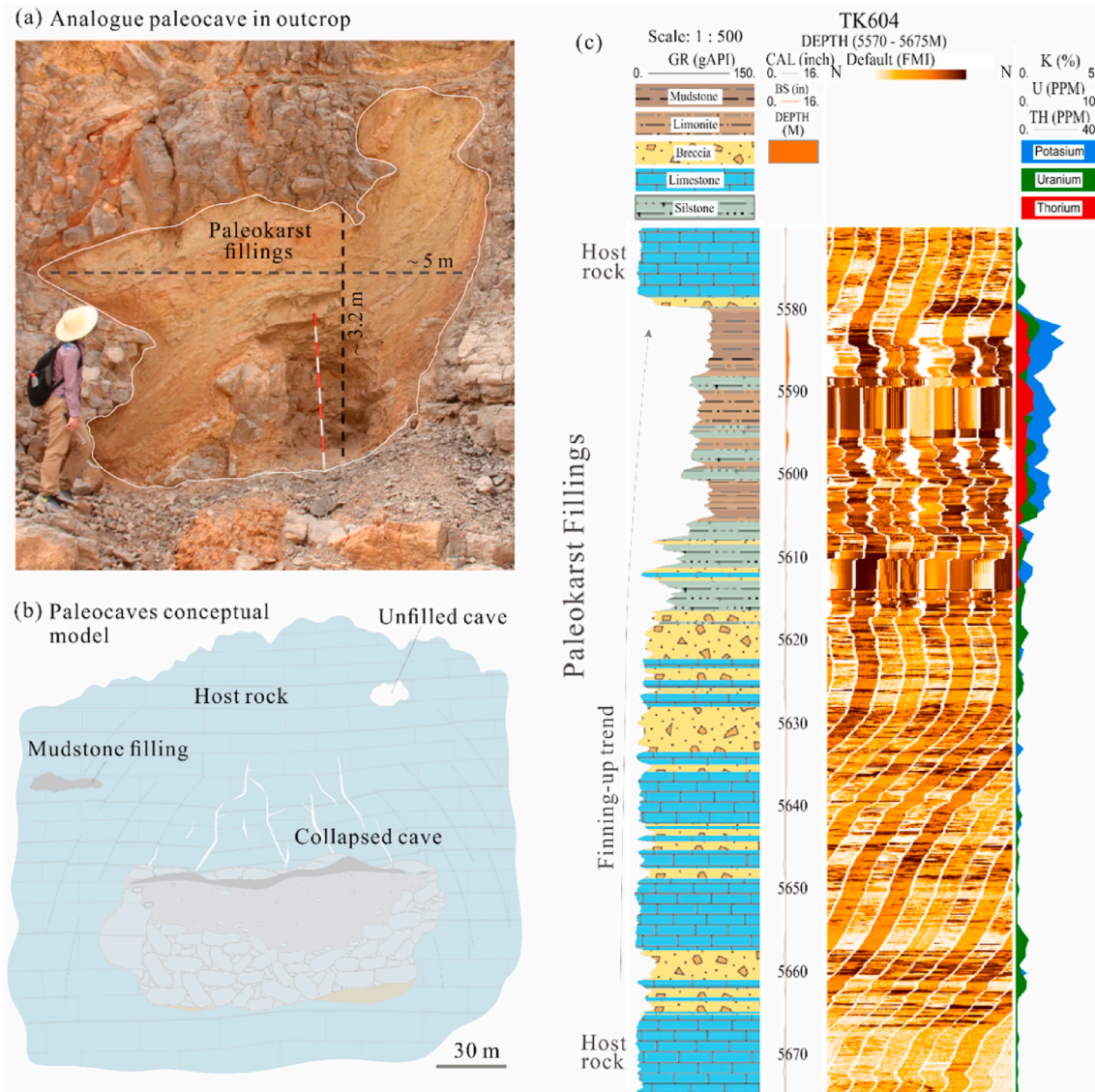


Fig. 5. Paleokarst fillings model; (a) Photo from an analogue of paleocave filled by clastic rocks; (b) proposed conceptual model of paleokarst fillings within carbonate host rock (modified from Loucks and Anderson, 1985; Loucks, 1999; 2001); (c) Diagram of the vertical distribution of the fillings described in well log. Modified from Méndez et al. (2019).

and compositional characteristics of a particular rock interval are required as input data in the DNNA workflow. Multi-regression analysis is used to determine the electrofacies logs that fit within the value range of the training data set of selected wireline logs (i.e., independent variables). The multi-regression analysis is defined in the following equation:

tion:

$$y = B_1 * x_1 + B_2 * x_2 + \dots + B_n * x_n + A \tag{1}$$

where y is the discriminant facies (dependent variable); x_1 and x_2 are the

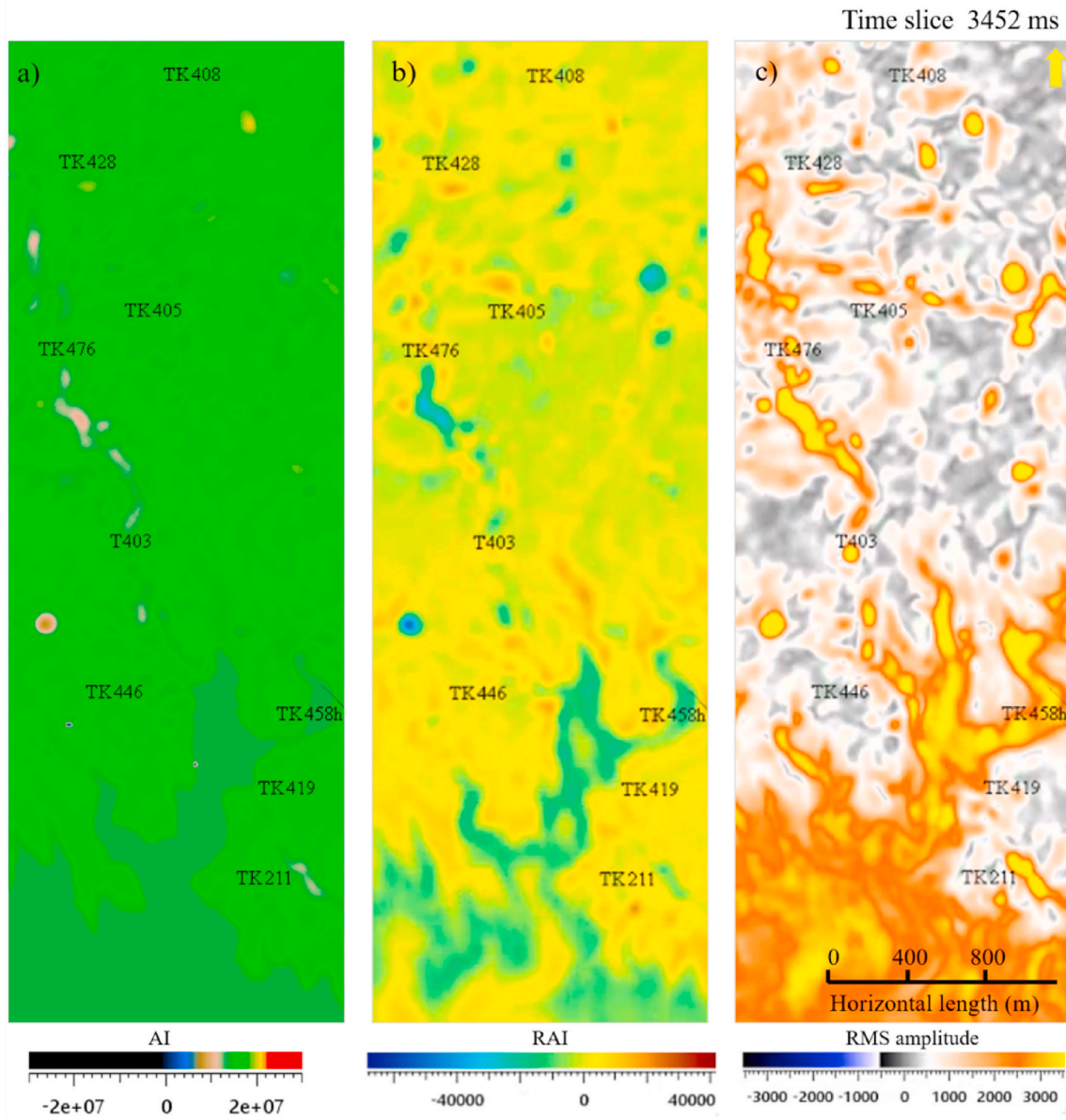


Fig. 6. The seismic attribute volumes selected for the DNNA processing technique: a) Acoustic Impedance, b) RAI; and c) RMS amplitude.

values of independent variables (well logs), and so on (x_n); and A and B are coefficients, linked to each independent variable.

Once the key curves are selected, they are trained and normalized in the petrophysical evaluation software (GEOLOG). The statistical distributions between curves of all selected wells are visualized in several cross plots. Then, the multi-regression analysis is applied to the data. The most representative electrofacies model is selected and then simplified based on the number of lithofacies defined from core and cutting sample descriptions.

3.2. Rock type prediction using the DNNA technique

A training set sample consist of pair variables, $T = (xw, C)$, where xw is defined by a d -dimensional vector x and a weight w being high for hard data and low for soft data (Hami-Eddine et al., 2015); and C is the index of lithological facies. For this case study, the data that have large weight (highly reliable) are those extracted and combined of the selected seismic attributes from impedance and amplitudes paired with the well information (Hami-Eddine et al., 2015). This technique simultaneously runs different neural networks to be trained with the same

hard data set (Zhou and Goldman, 2004). A statistical process of standardization is applied to the seismic attributes. Additionally, the introduction of soft data (democratic contribution) during the training process provides a stabilization effect on the result and reduces the bootstrap error rates. The soft data enriches the training data. The DNNA workflow is shown in Fig. 7.

In this study, we also apply the method proposed by Hami-Eddine et al. (2015) to validate the quality of output through the bootstrapping method. The bootstrap error computes by taking the “0.632+” estimator which is proposed by Hastie et al. (2009) and Hami-Eddine et al. (2015):

$$\widehat{Err}^{(0.632+)} = (1 - \widehat{\omega})\overline{err} + \widehat{\omega}\widehat{Err}^{(1)} \quad (2)$$

where, \overline{err} is the misclassification rate; $\widehat{\omega}$ is a weighting factor: $\widehat{\omega} = 0.632/(1-0.368\widehat{R})$; \widehat{R} is the relative overfitting error:

$$\widehat{R} = (\widehat{Err}^{(1)} - \overline{err}) / (\widehat{\gamma} - \overline{err}) \quad (3)$$

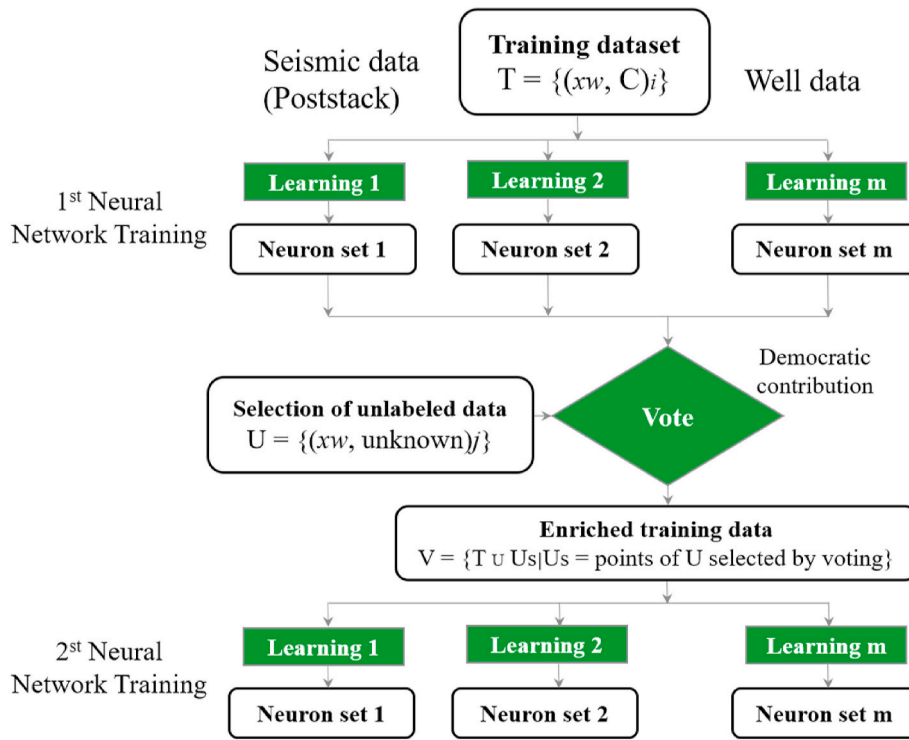


Fig. 7. Description of DNNA training steps for rock type prediction. Modified from Hami-Eddine et al. (2015).

$$\hat{\gamma} = \sum_{i=1}^C \hat{P}_i (1 - \hat{q}_i) \quad (4)$$

where, $\hat{\gamma}$ is the no-information rate; \hat{P}_i the proportion of responses; y_i corresponding to i ; \hat{q}_i is the computed proportion of predictions $\hat{f}^l(x_i)$ equaling i , and “ C ” represents the number of classes. However, the value \overline{Err} is the bootstrap error only for predictions from bootstrap samples that do not contain the x_i observation.

$$\widehat{Err}^{(l)} = \frac{1}{N} \sum_{i=1}^N \frac{1}{|C_{-i}|} \sum_{j \in C_{-i}} 1 - \delta_{y_i \hat{f}^l(x_i)}, \quad (5)$$

where, C_{-i} corresponds to set of indices of bootstrap samples that do not contain observation i ; $|C_{-i}|$ is the number of such samples; $\hat{f}^l(x_i)$ is the class prediction made by the network trained with the l th bootstrap set; and y_i is the expected answer. After implementation, the efficiency of the bootstrap error is evaluated from 0 to 100%.

To classify based on the most likely facies and, therefore, propagate neural network properties over the entire area of interest, we use a probabilistic version of K nearest neighbor algorithm (non-parametric). In this version, the weighting function is a Gaussian. The combination of K nearest neighbor algorithm with a Gaussian approach enables to calculate the distance between data points based on probability estimations (Specht, 1990; Hami-Eddine et al., 2015). The weight used for each neighboring point is weight = e-distance. This algorithm is expressed by the following equation:

$$P_{(c|y)} = \frac{\frac{1}{n_{k_c}} \sum_{i=1}^{n_{k_c}} \exp\left(-\frac{y-x_{(i)}^c}{2\sigma^2}\right)}{\sum_{j=1}^C \frac{1}{n_{k_j}} \sum_{i=1}^{n_{k_j}} \exp\left(-\frac{y-x_{(i)}^j}{2\sigma^2}\right)}, \quad (6)$$

where $P_{(c|y)}$ is the probability that y belongs to class c ; n_{k_c} is the number of codebook vectors of class c in the k -size neighborhood; σ is a smoothing parameter, and $x_{(i)}^c$ is the i th nearest training sample of class c

to y . This algorithm allows us to determinate the probabilities associated with each filling facies.

As the current computation is dot by dot processing, this investigation applies a structural smoothing to the probability volume using external Dip/Dip Azimuth attributes. It means, for each sample of the trace a dip-consistent plane which intersects the trace at that sample is constructed. This Dip-Steering processing has been adapted in order to use linear interpolation to track the seismic event. In addition, the smoothing filter used is the uniform mean.

3.3. 3D facies modeling

A geocellular grid in time is implicitly constructed between seismic horizons of the T_{74} and T_{76} unconformities (karsted interface) with the upscaled data from 10 wells located within the study area. Structural interpretation features are also considered in this model by evaluating their relationships with distribution fillings. After pairing the markers with the unconformity surfaces (horizons) and defining the fault intersections, the 3D structural model is generated in the software. That is, the framework skeleton of the carbonate platform is built.

Subsequently, we computed a geostatistical simulation using the Sequential Gaussian Simulation method (SGS). This method is a commonly used technique in oil and gas industry to simulate a subsequent grid point using the conditional distribution of observed variables. With SGS, data is first transformed to a Gaussian distribution so that the stationary histogram is Gaussian or normal. The simulated value at any given point is sampled from a Gaussian probability distribution. Furthermore, we condition the simulation to hard data, in this case, to the probable facies volume obtained from the DNNA technique. Through a stochastic process, this data is assigned to variables related to filling facies within grid as secondary input in the software trend analysis. This input allows generating a probabilistic volume that orients and propagates each facies in question. In this way, we condition the trends of fillings to adequate hard data. Finally, we compare the predicted and modeled facies. We do this by using the facies interpreted in those wells that were not considered in the workflow for validation of the predicted

results.

4. Results

The results obtained from rock type prediction and 3D facies modeling for each clastic filling are described below. Furthermore, we present addition the minor step by step procedures that were performed to estimate the electrofacies logs and build the geocellular grid. The realization shown is the closest to the analogue model.

4.1. Electrofacies logs result using multi-regression analysis

In the karsted carbonate intervals, we identified a total of 8 facies that were organized in the following order: limestone (host rock), siltstone, grained-fine sandstone, conglomerate, siliciclastic-carbonate mixture, mudstone, dolomite, and unfilled or empty. Moreover, the GR, RD, CNL, DEN, AC, PHIE and Perm curves were selected for the Multi-regression analysis training set, based on their responses or deflections

in karst interval. Then, these curves were effectively trained and normalized using petrophysical software. Through multiple cross charts computed the relationships between the different curve values (Fig. 8). The outcome of multi-regression analysis is simplified and adjusted to the 8 previously described lithofacies facies (Fig. 9). The resulting model is calculated the electrofacies log showing each facies.

4.2. Rock type prediction using the DNNA technique

After the electrofacies logs processing, they were paired with three selected seismic attributes (acoustic impedance, RAI, and RMS amplitude) which form our own hard data. Fig. 10 shows the result of developed training dataset. It was run on 6 neural networks with the selected hard data undergoing 30 interactions. Table 1 shows population repartition values for each facies or class obtained from the training set. Fig. 10 highlights a predicted log output calculated from reconstruction rates applied to well T403. The output is in agreement with the upscaled facies log. This figure also displays the maximum probability associated

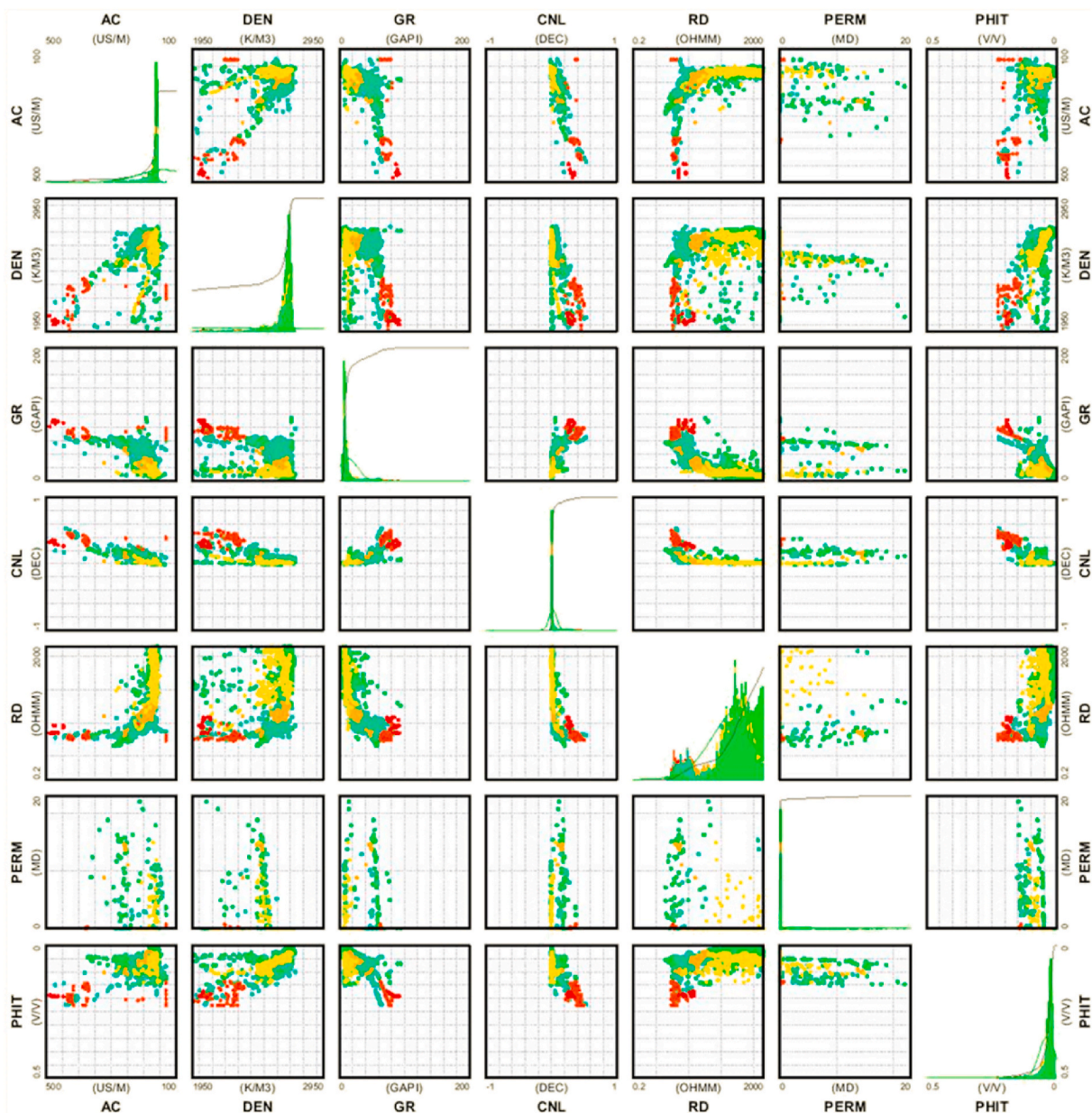


Fig. 8. Clustering associated with the dependent variable values through several cross plots.

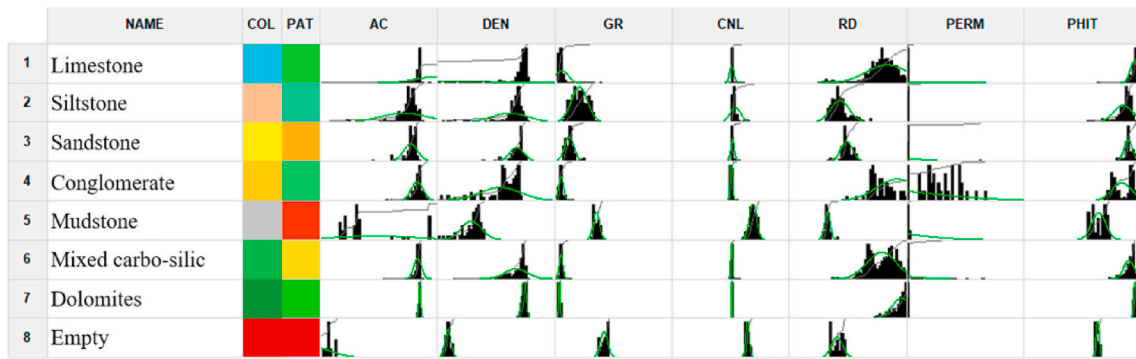


Fig. 9. Simplified result of multi-regression analysis applied to well logs. The colors of PAT track are showed according to prior clustering. In this figure, we relate the simplified result with each type of filling facies (COL track). (For interpretation of the references to color in this figure legend, the reader is referred to the Web version of this article.)

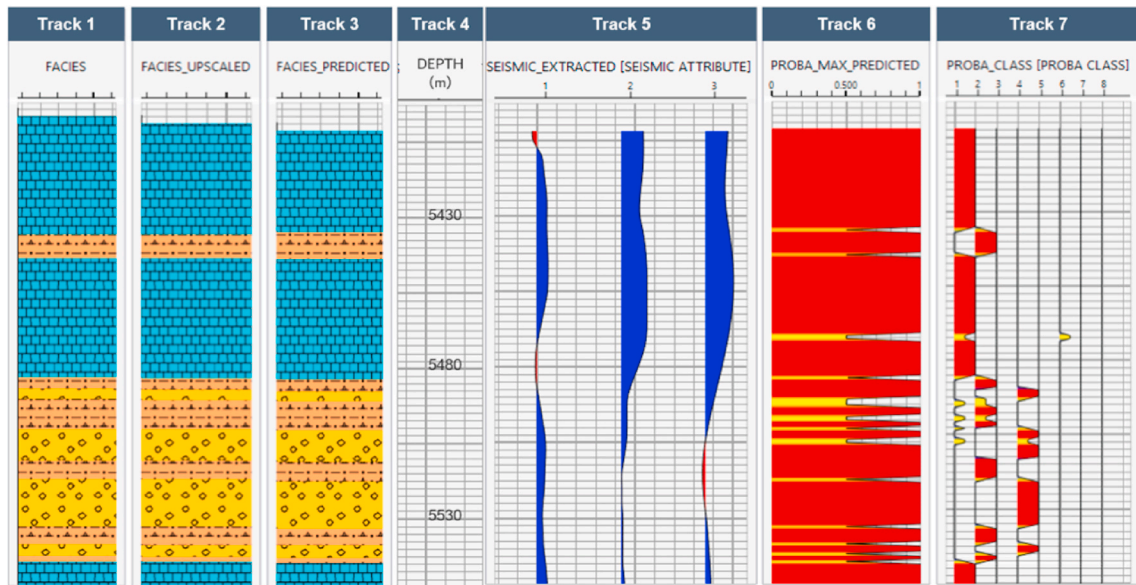


Fig. 10. The reconstruction rate of well T403. The tracks along the wellbore indicate the following: (1) Facies log; (2) Upscaled facies log; (3) Facies predicted; (4) Extracted seismic traces of involve poststack attributes; (5) The associated maximum probability with predicted facies log; and (6) Probability of traces per defined classes.

Table 1

Training set population repartition.

Parameters:

Number of Classes: 8

Training Set Dimension: 3

Window Length: 2 m

Vertical Sampling: 1 m

	Class							
	Class 1	Class 2	Class 3	Class 4	Class 5	Class 6	Class 7	Class 8
Repartition	85% (1965/2318)	3% (66/2318)	1% (34/2318)	4% (93/2318)	2% (44/2318)	3% (76/2318)	1% (32/2318)	0% (8/2318)

with the predicted facies log. It demonstrates high confidence in the prediction and the computed probability of traces per defined classes.

Moreover, for quality control of the DNNA predictive capabilities, the results are promising according to the low calculated bootstrap (training) error and rate classification. The obtained values are around 0.05 and 93.41%, respectively. The reconstruction rates matrix and summary of results is displayed in Table 2. The prediction quality outcome is satisfactory with good reconstruction rates at wells.

Nevertheless, some thin beds could not be reconstructed with their exact thicknesses. Detailed facies differentiation of paleokarst fillings using the DNNA training was possible.

Following the classification process, the probability of facies distribution was calculated to generate the probabilistic volume. In this case, each value at a given position corresponds to the most probable facies predicted. Fig. 11 shows an improved outcome by applying structural smoothing to the facies probabilistic volume, refining the details of

Table 2
Reconstruction rates matrix.

Training Summary
 Number of Neural Networks: 6
 Number of iterations: 30
 Well Prediction

Alpha Min: 0.001
 Alpha Max: 0.3
 Window Width: 0.1
 Epsilon: 0.1

Well	Class									All Classes
	Class 1	Class 2	Class 3	Class 4	Class 5	Class 6	Class 7	Class 8		
T403	99% (147/148)	100% (38/38)	N/A	100% (36/36)	N/A	N/A	N/A	N/A	N/A	100% (221/222)
TK210	99% (177/179)	N/A	N/A	N/A	96% (24/25)	N/A	N/A	N/A	N/A	99% (201/204)
TK211	100% (175/175)	100% (2/2)	100% (4/4)	N/A	N/A	100% (16/16)	N/A	N/A	N/A	100% (197/197)
TK405	100% (260/260)	100% (4/4)	N/A	N/A	N/A	100% (11/11)	N/A	N/A	N/A	100% (275/275)
TK408	100% (115/115)	N/A	93% (28/30)	N/A	N/A	100% (8/8)	97% (31/32)	N/A	N/A	98% (182/185)
TK419	98% (121/123)	67% (2/3)	N/A	100% (3/3)	100% (17/17)	0% (0/1)	N/A	100% (3/3)	N/A	97% (146/150)
TK428	100% (190/190)	N/A	N/A	N/A	N/A	N/A	N/A	N/A	N/A	100% (190/190)
TK446	100% (191/191)	N/A	N/A	N/A	100% (2/2)	95% (18/19)	N/A	N/A	N/A	100% (211/212)
TK458h	100% (495/495)	17% (1/6)	N/A	100% (25/25)	N/A	100% (21/21)	N/A	N/A	N/A	99% (542/547)
TK476	100% (89/89)	85% (11/13)	N/A	97% (28/29)	N/A	N/A	N/A	100% (5/5)	N/A	98% (133/136)
All Wells	100% (1960/1965)	88% (58/66)	94% (32/34)	99% (92/93)	98% (43/44)	97% (74/76)	97% (31/32)	100% (8/8)	N/A	99% (2298/2318)

Number of stable points: 23230
 Percent of stable data well classified: 98.347%
 Bootstrap (training) error: 0.0505176
 Bootstrap classification rate: 93.4148 %

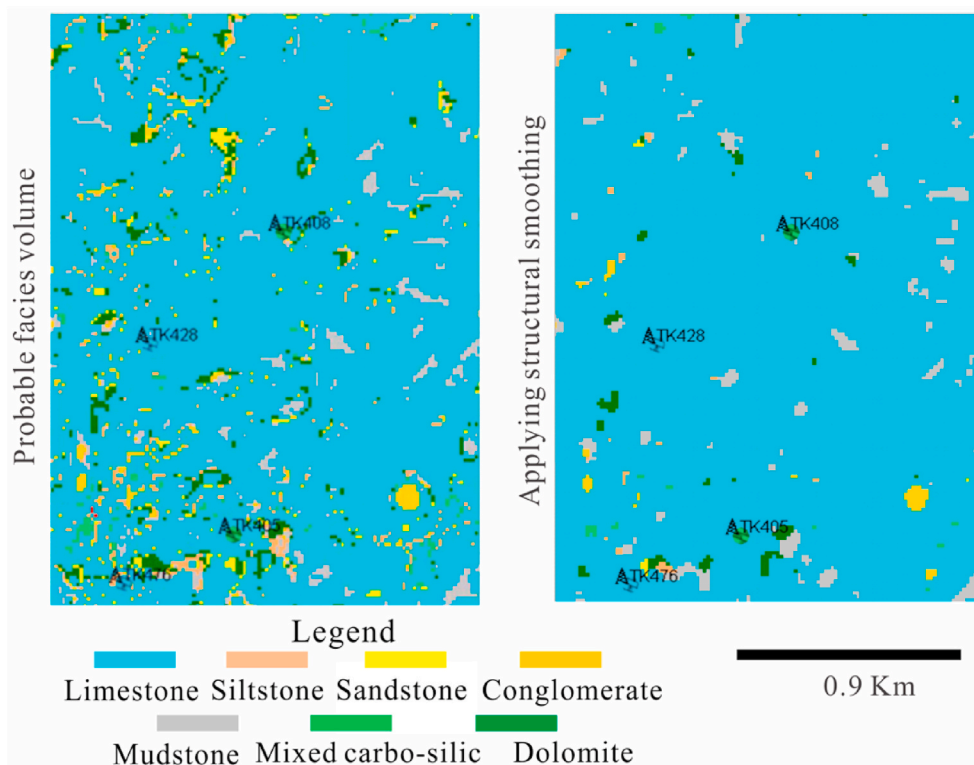


Fig. 11. The improvement obtained by applying structural smoothing in the facies probabilistic volume. It is evident that the technique eliminates all those features that are not related to paleokarst or noise.

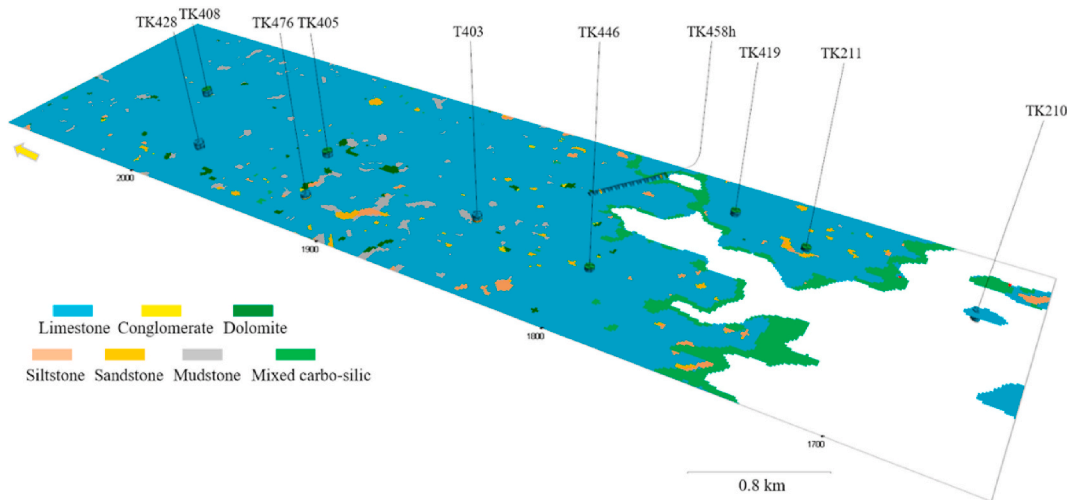


Fig. 12. The most probable facies volume obtained using the DNNA technique in rock type prediction. In this slice, we show the good reconstruction of clastic filling facies in accordance with the karst morphology.

filling patterns.

The outcome is displayed on a time slice in Fig. 12. In this figure, clastic fillings are patchily distributed owing to the influence of paleotopography of karst systems by keeping the same trajectories as the cavities. These lithofacies agree with the karst elements recognized in seismic attribute on the same time slice. The unfilled cavities (empty) outputs were very scarce due to their low probability in the DNNA computed. Consequently, this probabilistic analysis cannot be conclusive for this type of karst feature.

A cross section generated from the probable facies volume in the northeast–southwest direction (Fig. 13) shows that the sorting or internal configuration of fillings within chambers can be observed in detail. The figure highlights mudstone facies interbedded with siltstone and mixed siliciclastic and carbonate. These predicted facies were validated by the well logs. However, we observe that the lateral continuity is weak, which is likely related to the rock type (e.g., limestones) and low seismic resolution. The features described in this cross section were also directly observed on with the seismic amplitude attribute. This shows the capacity of the DNNA technique to capture the discrete fillings. In addition, heterogeneous facies (i.e., calcarenite) at the upper sections were recognized and associated with weathering crust.

4.3. 3D facies modeling of clastic fillings and host rock

Once the most probable facies volume is computed, a grid is constructed for the study area. In Fig. 14, we display the workflow that involve the construction phases for a fine-scale geocellular grid (i.e., faults and horizons modeling). This process involves, an interpreted structural model formed by 11 faults (between strike-slip and reverse faults) with very fine layering. For this case study, 7 of the 8 facies interpreted from the fillings and the host rock were picked in well logs and upscaled into the simulation grid. The proportion of each upscaled facies is shown in the histogram of Fig. 15.

Subsequently, the probability of clastic filling facies was estimated using the prior probable facies model as input data. This robust method combines estimated seismic attribute volumes and populates the occurrence of the facies, cell by cell in accordance with karst morphology (Fig. 16). Particularly, those facies with higher probability in the data analysis, for example limestone, conglomerates, mixed carbonates – siliciclastic, and siltstones were clearly delineated in both horizontal and vertical direction. It is evident that the probability of occurrence of limestone is the highest (>0.8) due to it being the host rock (Fig. 16). The high probability of mixed carbonates – siliciclastic specifically in the upper part is consistent with deposition characteristics. In contrast, the probability occurrence of shale, dolomite, and

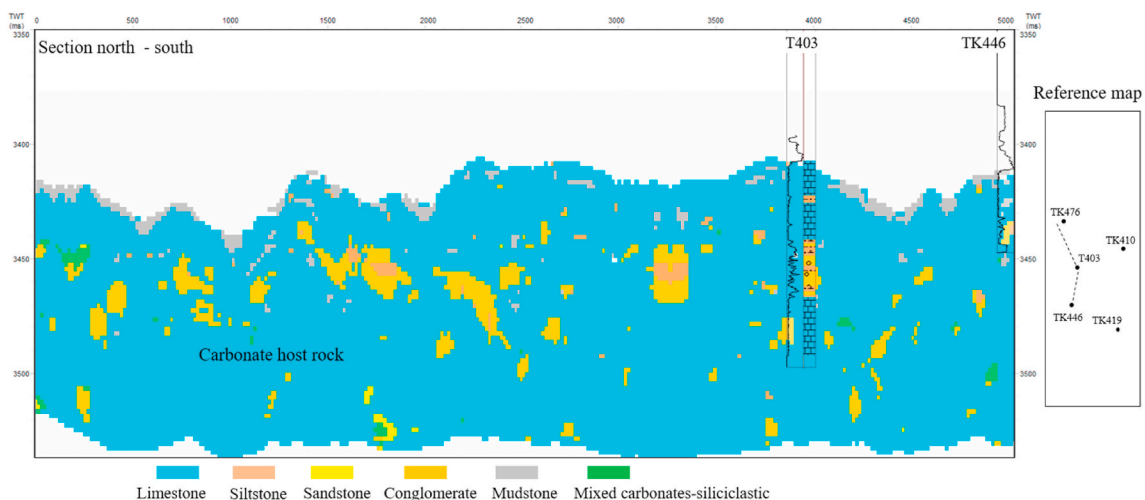


Fig. 13. Showing a cross section oriented north – south obtained from probable facies volume.

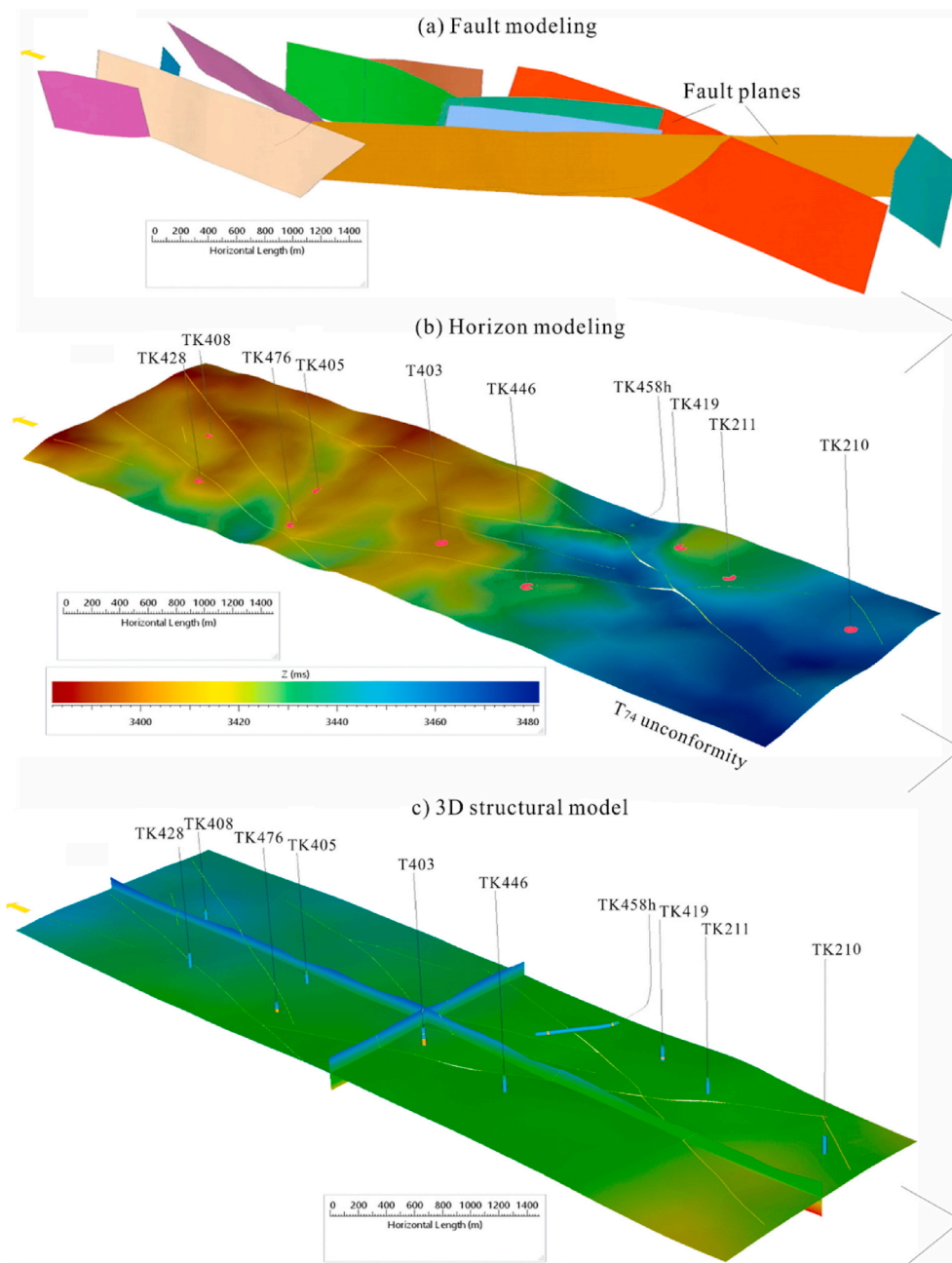


Fig. 14. Simple workflow covering the following components: (a) 11 faults that involve the fault modeling; (b) horizon model at T₇₄ unconformity level; and (c) 3D structural model outcome.

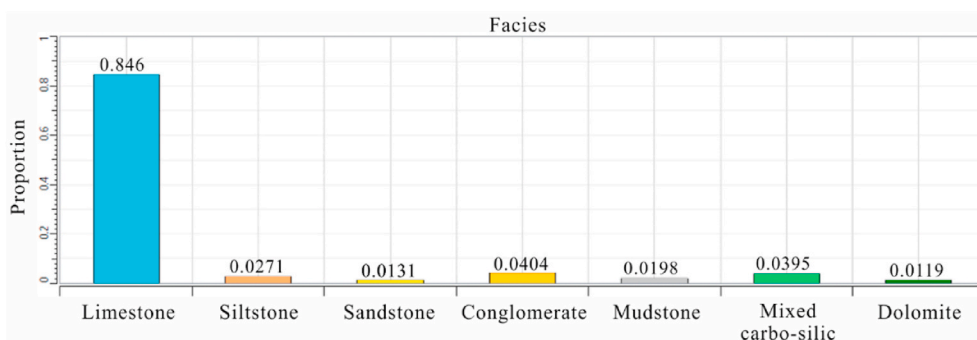


Fig. 15. Proportion histogram of upscaled facies statistically computed in the geocellular grid.

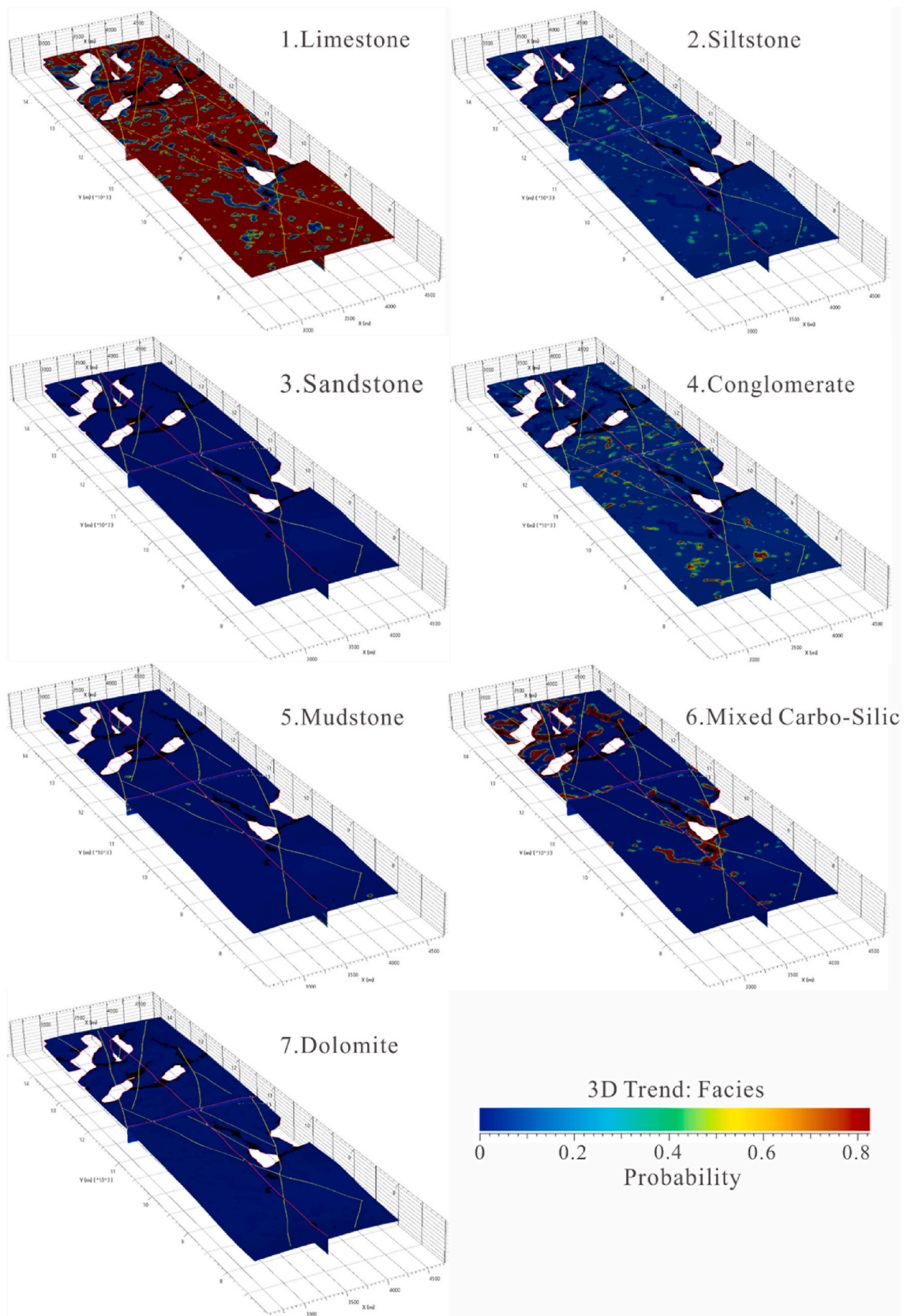


Fig. 16. Probabilities volume by facies obtained from trend data analysis.

sandstone facies was only conditioned in those regions very close to the well data.

After conditioning the fillings facies and using the SGS geostatistical method, a first realization is processed and shown in a cross section (Fig. 17). Fig. 17 highlights good vertical delineation and spatial distribution of paleokarst fillings according to karst morphology (i.e., caves and sinkholes) within the fine-scale geocellular grid.

Fig. 18 displays two slices showing the top and intermediate sections of the model with the detailed main features of clastic fillings in a geocellular grid. Even the computed facies get the same patchy distribution of lithofacies patterns visualized in the probable facies volume. Particularly, Fig. 17a highlights similar geometries to river channels which are associated with the sedimentation of mixed carbonate and siliciclastic at top of model. This agrees with proposed models by several researchers on epikarst deposits (Jin et al., 2015a; Wu et al., 2018). In addition to Fig. 17b, the fillings that are hosted within paleocaves (run-off subzone) have been modeled in accordance with patterns and shapes interpreted in seismic dataset.

5. Discussion

5.1. DNNA versus previous models/results

Artificial neural networks and 3D facies modeling are significant methods for addressing complex problems related to geosciences (Elshafei and Hamada, 2007; Alkinani et al., 2019). We integrated these methods to obtain increasingly realistic realizations of the karst system in Ordovician carbonate reservoirs. To this end, we have computed a probable facies volume obtained from the DNNA technique. This volume provides a spatial distribution of the highly heterogeneous clastic paleokarst fillings hosted in the cavities.

Moreover, we have followed a similar workflow proposed by Méndez et al. (2019) to predict paleokarst fillings in a nearby area. However, we have considerably improved the patterns predictions by using more core samples descriptions and other curves as input in the multi-regression analysis (e.g., total porosity and permeability). The lithology distribution analysis of clastic filling facies performed in the 10 available wells permitted the discrimination by lithofacies of fillings. Total porosity (PHIT) and permeability (Perm) curves were added to the feature set and improved the statistical distribution of electrofacies logs.

In summary, the application of the DNNA technique for rock type prediction demonstrated promising results in computing facies proportions in a voxel despite the high heterogeneity of fillings. The low value of the bootstrap (training) error and the high percentage rate of classification (around 0.05 and 93.41%, respectively), suggests that the

data used fulfilled the basic requirements for an effective evaluation. However, we can increase this percentage if there were more data from wells. Moreover, the DNNA technique identified important siltstones or fine-grained sandstone patterns surrounding the main faults which could be excellent hydrocarbons reservoirs due to their structural positions. We also observed some gaps in the continuities of conglomerate or breccia fillings in the probable facies volume. This observation is because, in some instances, these fillings have the same seismic response as the carbonate host rock. The empty facies also indicate underestimation in the most probable facies volume, due to their low resolution in seismic dataset and well logs. Therefore, this facies with a <0.001% proportion could not be modeled without negatively impacting the results.

Despite the limited scope of data, there was a coherent prediction of the shallowest lithofacies which have good continuity (i.e., mudstone and mixed carbonate–siliciclastic). The geometry of mixed carbonate–siliciclastic fillings related to calcarenites clearly matches with the geometry of rivers on the platform or underground streams in the cavities (Zeng et al., 2010). On the other hand, the DNNA technique did not reveal any feature related to collapsed cavities with fillings (Loucks and Anderson, 1985; Loucks, 1999, 2001). The DNNA's probabilistic approach represents a starting point for estimating many other rock properties (i.e., porosity, permeability, fluids flow, etc.).

5.2. Reliability of facies model

Concerning the 3D modeling, the fine-scale geocellular grid was constructed with the spatial dimensions $10 \times 10 \times 1$ m because this was the minimum dimension that the software permitted for the computation on the simulation grid. Nevertheless, we considered that the spatial dimensions should be smaller around $5 \times 5 \times 1$ m, according to the analogue model. The 3D facies model computed using the SGS algorithm respected the proportions of each facies calculated from the most probable facies volume. The low probabilities of dolomite and sandstone facies result from the poor occurrence of these rocks in interpreted well logs.

The 3D model outputs are relatively consistent with the conceptual model proposed for the study area where the paleocaves and fillings maintain the same orientation as the main striking faults (Fig. 18). Therefore, a sound understanding of the platform's tectonic dynamic evolution could determine how the cavities were first generated. The sediment sourcing that dominants from the northwestern-southeastern. The lateral and vertical lithofacies changes of the fillings show similar characteristics with the sorting observed in analogue cavity model (Fig. 5a). Finally, this last observation supports studies (Tian et al.,

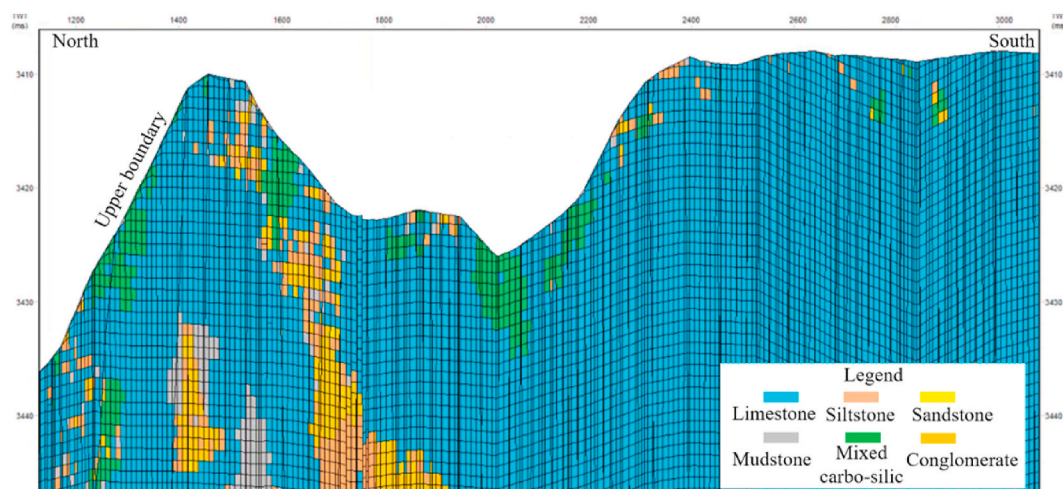


Fig. 17. Geocellular grid populated by the filling facies in which highlights a good correlation with conceptual model of sinkholes and caves.

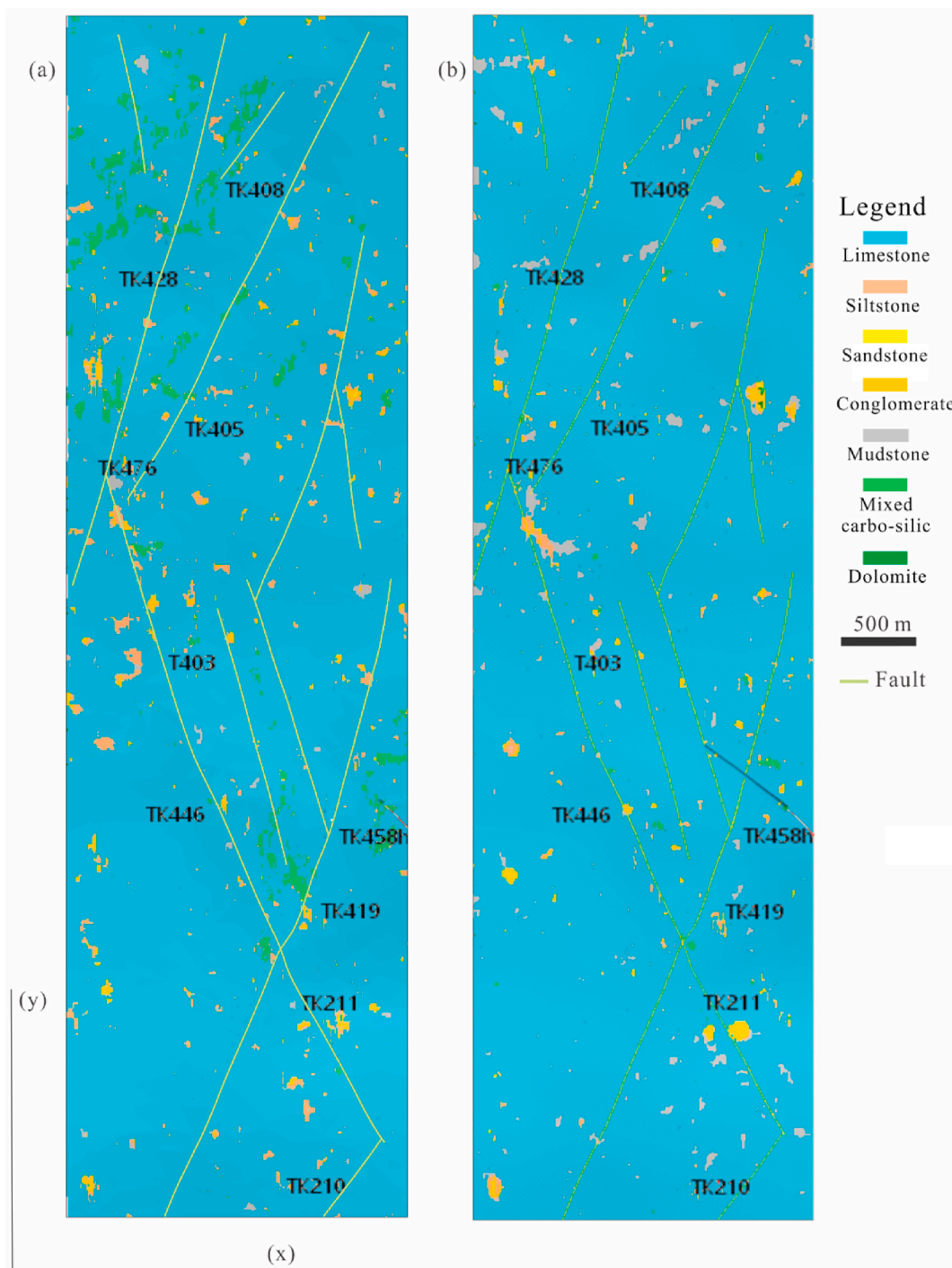


Fig. 18. Two slices showing the results from the static model: a) upper section where the highest proportion of mixed carbonate – siliciclastic facies is noted; b) intermediate section in which the logical distribution of paleokarst facies is denoted.

2016; Méndez et al., 2020 a) propose that fillings occur solution-enlarged fractures in carbonates.

5.3. Model validation

For validation, we compare the predicted and modeled facies to the facies interpreted along the wellbore of well TK411 (Fig. 19). In Fig. 19, we observed a significant correlation between the interpreted and predicted facies (correlation percentage around 73.6%; tracks 2 and 3, respectively), demonstrating the DNNA technique’s effectiveness. However, we also detect that the technique overestimated the mixed

carbonate-siliciclastic facies (green color) in karsted interval. This defect is related to similar features that the facies mentioned above have with the siltstone lithofacies (light brown color).

6. Conclusions

We demonstrated that the DNNA technique probabilistically predicted the distribution and sorting of clastic fillings hosted within carbonates in accordance with well data and seismic datasets. The total porosity (PHIE) and permeability (Perm) measurements combined with other features improved our predictions’ accuracy. The result obtained

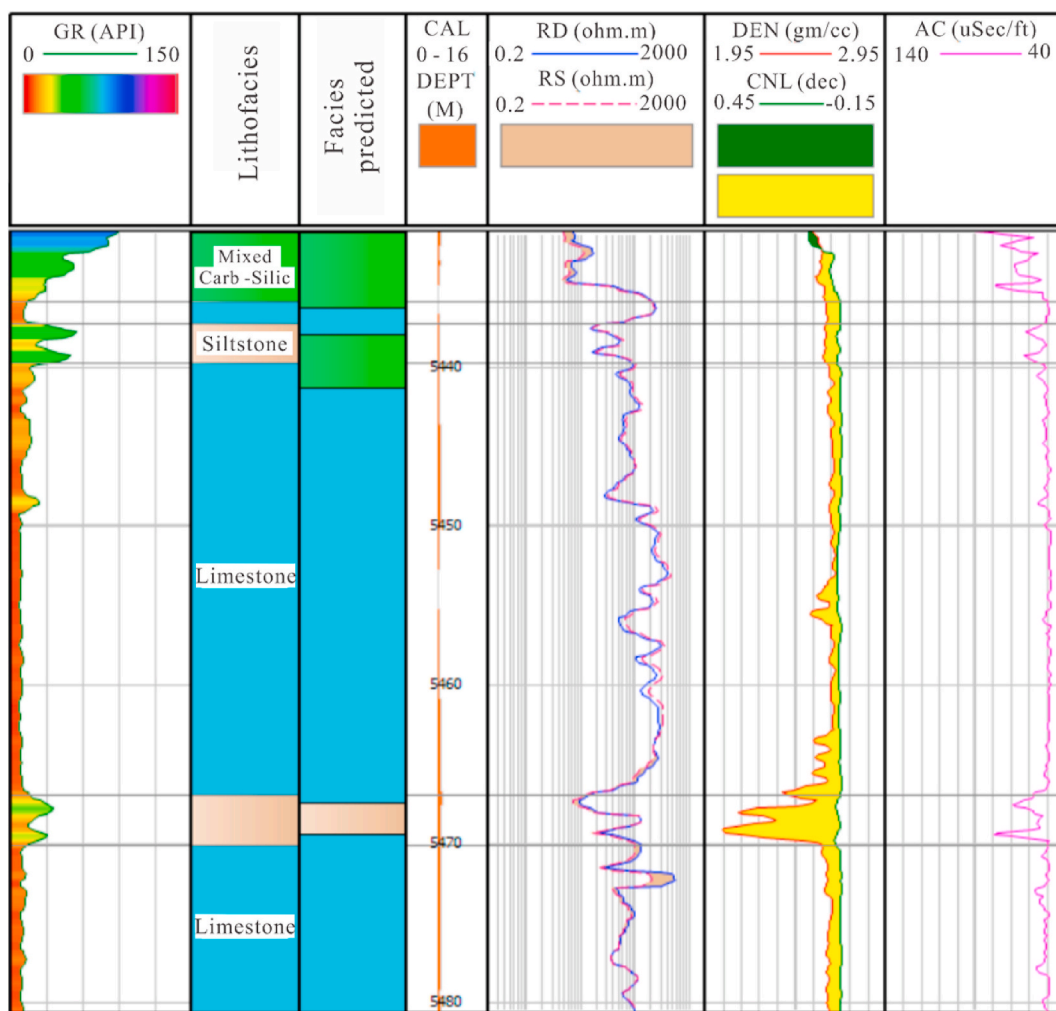


Fig. 19. Well logs of well TK411 paired with the facies predicted from the DNNA technique. The figure highlights the agreement of the typical facies with respect to the previously defined lithofacies.

from the probable facies volume was used to construct the facies modeling based on the accurate delineation of the clastic fillings' patterns. Trend analysis supports the estimation of each facies or class obtained. In this way, this technique allows for the improvement of the facies modeling to generate a more realistic realization of the models.

Finally, the resulting 3D model highlights the occurrence of large patches of siltstone or fine-grained sandstone fillings in regions near the main faults, east of the study area. These fillings are sometimes quite attractive patterns for optimizing oil exploitation in the area, due to their good physical characteristics (i.e., porosity and permeability). The characteristics related to connectivity and distribution of patterns are still a complex issue to evaluate. However, the predicted and modeled facies correctly honored the prior geological interpretation.

Credit author statement

Jose N Mendez: Conceptualization, Methodology, Software, Visualization, Investigation and Writing-Original draft preparation. Jin Qiang.: Conceptualization, Data curation, Writing – original draft preparation. Xudong Zhang: Software, Visualization, Investigation. Maria Gonzalez: Software, Visualization. Muhammad Kashif: Writing – original draft preparation. Cyril D. Boateng and Miller Zambrano: Writing- Reviewing and Editing.

Declaration of competing interest

The authors declare that they have no known competing financial interests or personal relationships that could have appeared to influence the work reported in this paper.

Acknowledgments

The manuscript is part of the first author's Ph.D. thesis. This work was supported by the National Scientific Funding Project (U1663204), the National Key Scientific Project (2016ZX05014-002), and PetroChina Scientific Funding (2016B-0401). The authors are grateful to China Petroleum and Chemical Corporation (SINOPEC) for permission to use the data in this paper.

References

Alberty, m.w., 1994. Standard interpretation; part 4-wireline methods. In: Morton-Thompson, D., Woods, A.M. (Eds.), Development Geology Reference Manual: AAPG Methods in Exploration Series 10, pp. 180–185.
 Ali, J.K., 1994. Neural networks: a new tool for the Petroleum industry?. In: Paper in Presented at European Petroleum Computer Conference. SPE-10.2118/27561-MS.
 Alkinani, H.H., Al-Hameedi, A.T.T., Dunn-Norman, S., Flori, R.E., Alsaba, M.T., Amer, A. S., 2019. Applications of artificial neural networks in the Petroleum industry: a review. In: Paper Presented at SPE Middle East Oil and Gas Show and Conference, Manama, Bahrain. SPE-10.2118/195072-MS.

- Boateng, C.D., Fu, L., Danuor, S.K., 2020. Characterization of complex fluvio-deltaic deposits in Northeast China using multimodal machine learning fusion. *Sci. Rep.* 10, 13357.
- Changsong, L., 2011. Tectonic framework and paleogeographic evolution of the Tarim basin during the Paleozoic major evolutionary stages. *Acta Petrol. Sin.* 27 (1), 210–218.
- Chen, D., Wei, X., 2010. Well logging evaluation on fractured carbonate reservoirs in Tahe area. *Petroleum and Geophysical Exploration* 49, 147–152.
- Chen, J., Zeng, Y., 2018. Application of Machine Learning in Rock Facies Classification with Physics-Motivated Feature Augmentation. *Machine Learning, Geophysics*. 1808.09856.
- Chen, Q., Zhao, Y., Li, G., Chu, C., Wang, B., 2012. Features and controlling factors of epigenetic karstification of the ordovician carbonates in akekule arch, Tarim basin. *J. Earth Sci.* 23 (4), 506–515. \.
- Chevitarese, D.S., Szwarcman, D., Silva, R.M., Brazil, E.V., 2018. Deep learning applied to seismic facies classification: a methodology for training. *Comp. Sci.*
- Chunyan, L., 2008. Burial dissolution of ordovician granule limestone in the Tahe oilfield of the Tarim basin, NW China, and its geological significance. *Acta Geol. Sinica-Eng. Edn.* 82 (3), 520–529.
- Dell'oca, S., 1961. Rimpimenti naturali di grotte: Como, Italy. *Rassegna Speleologica Italiana*, p. 277.
- De Ribet, B., 2016. Integrating well and seismic data for rock type prediction using a Democratic Neuronal Network Association approach. In: Presented at AAPG Middle East Geosciences Technology Workshop, Advances in Subsurface Imaging and Mapping. Muscat, Oman. Article N° 90286.
- Di, H., Gao, D., Alegrib, G., 2019. Developing a seismic texture analysis neural network for machine-aided seismic pattern recognition and classification. *Geophys. J. Int.* 218, 1262–1275.
- Elshafei, M., Hamada, G.M., 2007. Neural network identification of hydrocarbon potential of shaly sand reservoirs. In: Society of Petroleum Engineers. Paper Presented at SPE Saudi Arabia Section Technical Symposium. SPE-10.2118/110959-MS.
- Hall, B.J., 2016. Facies classification using machine learning. *Lead. Edge* 35 (10), 906–909.
- Hami-Eddine, K., Klein, P., Richard, L., De Ribet, B., Grout, M., 2015. A new technique for lithology and fluid content prediction from prestack data: an application to a carbonate reservoir. *Interpret.* J. 3 (1), 19–32.
- Hastie, T., Tibshirani, R., Friedman, J., 2009. *The Elements of Statistical Learning*, second ed. Mumbai: Springer-Verlag, New York, p. 745.
- He, Z., Peng, S., Zhang, T., 2010. Controls on reservoir formation in ordovician of Tahe oilfield, Tarim basin, and combinational genetic mechanism. *Oil Gas Geol.* 31 (6), 743–752.
- Jin, Q., Kang, X., Rong, Y., Tian, F., 2015a. Sedimentary and geochemical characteristic of sandstone and mudstones deposited in surface rivers and subsurface rivers in Ordovician Karsted carbonates. Tahe Oilfield. *J. China Univ. Petrol. (Edn. Nat. Sci.)* 39 (6), 1–10.
- Jin, Q., Tian, F., Lu, X., Kang, X., 2015b. Characteristic of collapse breccia filling in caves of runoff zone in the Ordovician karst in Tahe oilfield, Tarim Basin. *Oil Gas J.* 36 (5), 729–735.
- Kong-A-Siou, L., Johannet, A., Borell Estupina, V., Pistre, S., 2015. Neural networks for karst groundwater management: case of the Lez spring (Southern France). *Environ. Earth Sci.* 74, 7617–7632.
- Kovacević, M., Ivanišević, N., Dašić, T., Marković, L., 2018. Application of artificial neural networks for hydrological modelling in karst. *Gradevinar* 70 (1), 1–10.
- Li, B., Jia, C., Wang, W., Yu, C., Li, F., Liu, P., 2014. Characteristic and main controlling factors of karst caves in the Tarim basin. In: Poster Presented at: AAPG Annual Convention and Exhibition, Houston, USA.
- Li, Y., Hou, J., Li, Y., 2016. Features and classified hierarchical modeling of carbonate fracture-cavity reservoirs. *Petrol. Explor. Dev.* 43 (4), 655–662.
- Li, Y., 2017. Development Theories and Methods of Fracture-Vug Carbonate Reservoirs. Elsevier, China, p. 514.
- Li, Y., Kang, Z., Xue, Z., Zheng, S., 2018. Theories and practices of carbonate reservoirs development in China. *Petrol. Explor. Dev.* 45 (4), 712–722.
- Lin, Y.P., Wu, T.Z., Sheng, X.F., Wang, C.S., Zhou, T.W., 2013. Artificial neural networks identification of lithology-types in complex carbonate from well logs, block K, in Uzbekistan. *Adv. Mater. Res.* 756–759, 2396–2400.
- Liu, C., Lin, C., Wang, Y., Wu, M., 2008. Burial dissolution of ordovician granule limestone in the Tahe oilfield of the Tarim basin, NW China, and its geological significance. *Acta Geol. Sin.* 82 (3), 520–529.
- Liu, M., Jervis, M., Li, C., Nivlet, P., 2020. Seismic facies classification using supervised convolutional neural networks and semisupervised generative adversarial networks. *Geophysics* 85 (4), 57–58.
- Loucks, R.G., 1999. Paleocave carbonate reservoirs: origins, burial-depth modifications, spatial complexity, and reservoir implications. *AAPG (Am. Assoc. Pet. Geol.) Bull.* 83, 1795–1834.
- Loucks, R.G., 2001. Modern analog for paleocave-sediment fills and their importance in identifying paleocave reservoirs. *Gulf Coast Assoc. Geol. Soc. Trans.* 46, 195–206.
- Loucks, R.G., Anderson, J.H., 1985. Depositional facies, diagenetic terrains, and porosity development in lower ordovician ellenburger dolomite, pucket field, west Texas. In: Roehl, P.O., Choquette, P.W. (Eds.), *Carbonate Petroleum Reservoirs*. Springer-Verlag, pp. 19–38.
- Lu, X., Zhao, M., Hu, X., Jin, Y., 2012. Studies of 3D Reservoir modeling: taking Ordovician carbonate fractured-vuggy reservoirs in Tahe Oil Field as an example. *Petrol. Geol. Exp.* 34 (2), 193–198.
- Mazzullo, S., Chilingarian, G., 1996. Hydrocarbon reservoirs in karsted carbonate rocks. *Developments in Petroleum Science*, pp. 797–865.
- Mendez, J.N., Jin, Q., Gonzalez, M., Zhang, X., 2019. Rock Type Prediction Using Democratic Neural Networks Association DNNA: an Alternative Method to Describe Clastic Fillings in Ordovician Karsted Carbonates within a Region of the Tahe Oilfield. *OnePetro*, China, p. 11. SPE-197279-MS.
- Mendez, J.N., Jin, Q., Gonzalez, M., Zhang, X., Lobo, C., Boateng, C., Zambrano, M., 2020 a. Fracture characterization and modeling of karsted carbonate reservoirs: a case study in Tahe oilfield, Tarim Basin (western China). *Mar. Petrol. Geol.* J. 112, 17.
- C. Mendez, J.N., Jin, Q., Gonzalez, M., Wei, H., Boateng, C., 2020 b. Predicting and 3D modeling of karst zones using seismic facies analysis in Ordovician carbonates of the Tahe oilfield, China *Interpret.* J. 8 (2), 1–19.
- Morris, R.L., Biggs, W.P., 1967. Using log-derived values of water saturation and porosity: transactions of the SPWLA annual logging symposium. In: Paper X, P. 26. *Seismic Facies Classification and Identification by Competitive Neural Networks*.
- Saggaf, M., Nafi Toksoz, M., Marhoon, M., 2003. Seismic facies classification and identification by competitive neural networks. *Geophysics* 68 (6), 1984–1999.
- Shashank, S., Mahapatra, M.P., 2018. Boosting Rock Facies Prediction: Weighted Ensemble of Machine Learning Classifiers. *Society of Petroleum Engineers, OnePetro*, p. 17. SPE-192930-MS.
- Specht, D.F., 1990. Probabilistic neural networks. *Neural Network.* 3, 109–188.
- Tian, F., Jin, Q., Xinbian, L., Yuhong, L., Likuan, Z., Songqing, Z., Hongfang, Z., Yuanshuai, R., Naigui, L., 2016. Multi-layered Ordovician paleokarst reservoir detection and spatial delineation: a case study in the Tahe Oilfield, Tarim Basin, western China. *Mar. Petrol. Geol.* J. 69, 53–73.
- Tian, F., Lu, X., Zheng, S., Zhang, H., Rong, Y., Yang, D., Liu, N., 2017. Structure and Filling Characteristics of Paleokarst Reservoirs in the Northern Tarim Basin, Revealed by Outcrop, Core and Borehole Images, vol. 9. *De Gruyter Open*, pp. 266–280.
- Wu, J., Fan, T., Gao, Z., Gu, Y., Wang, J., Du, Y., Fan, H., 2018. Identification and characteristic analysis of carbonate cap rock: a case study from the Lower-Middle Ordovician Yingshan Formation in Tahe oilfield, Tarim Basin, China. *J. Petrol. Sci. Eng.* 164, 362–381.
- Xiao, Y., He, F., Sun, Y., 2003. Reservoir characteristic of paleocave carbonates a case of study Ordovician paleocave in Tahe Oilfield, Tarim Basin. *Oil Gas Geol.* 24 (1), 75–80.
- Yang, H., Sun, Z.D., Cai, L.L., 2011. A new method of Evaluation of formation for fractured and caved carbonated reservoirs: a case study from the Lundong area, Tarim Basin, China. *Petrol. Sci.* 8 (6), 446–454.
- Yu, J., Li, Z., Yang, L., Han, Y., 2018. Model identification and control of development of deeply buried paleokarst reservoir in the central Tarim Basin, northwest China. *J. Geophys. Eng.* 15 (2), 576–592.
- Zeng, H., Loucks, B., Janson, X., 2010. An ultra-deep paleokarst system in the ordovician, north-central Tarim basin, China: high-resolution 3D seismic interpretation. In: SEG Denver Annual Meeting, pp. 1526–1530.
- Zhang, W., Jin, Q., Xu, S., 2012. Paleocavern filling characteristic and hydrocarbon reservoir implication in the Ordovician outcrops in the northern Tarim Basin. *Special Oil Gas Reservoirs* 19 (3), 50–54.
- Zhao, M., Kang, Z., Liu, J., 2008. Modeling and application of fractured-vuggy carbonate reservoirs. *Xinjing Pet. Geol.* 29 (3), 318–320.
- Zhao, W., Shen, A., Qiao, Z., Zheng, J., Wang, X., 2014. Carbonate karst reservoirs of the Tarim Basin, northwest China: types, features, origins, and implications for hydrocarbon exploration. *Interpret.* J. 2 (3), 65–90.
- Zhao, T., 2018. Seismic facies classification using different deep convolutional neural networks. In: 88th Annual International Meeting. SEG, Expanded Abstracts, pp. 2046–2050.
- Zhou, Y., Goldman, S., 2004. Democratic Co-learning: Presented at 16th IEEE International Conference on Tools with Artificial Intelligence.